POLITECNICO DI TORINO
Repository ISTITUZIONALE

Receiver Sand Mitigation Measures along railways: CWE-based conceptual design and preliminary performance assessment

Terms of use:

Publisher copyright

(Article begins on next page)

29 April 2024

Receiver Sand Mitigation Measures along railways: CWE-based conceptual design and preliminary performance assessment

Marko Horvat [a], Luca Bruno [a,c,*], Sami Khris [b,c]

[a] *Politecnico di Torino, Department of Architecture and Design, Viale Mattioli 39, I-10125, Torino, Italy*
[b] *Optiflow Company, 160, Chemin de la Madrague-Ville, F-13015, Marseille, France*
[c] *Windblown Sand Modelling and Mitigation joint research group, Italy*

ARTICLE INFO

ABSTRACT

Desert railways are constantly exposed to incoming wind-blown sand. The railway structure locally disturbs the incoming sand drift, induces its accumulation, and ultimately suffers its harmful effects. Receiver Sand Mitigation Measures (SMMs) aerodynamically interact with the track system, induce sand erosion around it, and allow sand transport far downwind it. The conceptual and preliminary design of an innovative Receiver SMM called *Sand Blower* is developed in this study. The design is grounded on the aerodynamic behaviour of the baseline humped sleeper track system. The flow control strategy is intended to avoid boundary layer separation, and to promote local flow acceleration by means of the Venturi effect. The performance assessment is carried out by Computational Wind Engineering approach. It allows to simulate the local wind flow, to obtain the shear stress field at the wall, and to derive from it sand sedimentation, windward erosion and backward erosion conditions. The results show that the Sand Blower greatly increases the track system performance by reducing sand sedimentation and increasing sand erosion under wide range of wind speeds and directions.

1. Introduction

Desert railways locally disturb windblown sand drift and induce sand sedimentation and erosion around them. Because of accumulated sand, railways can attain Sand Serviceability Limit States (SSLS) and/or Sand Ultimate Limit States (SULS), as defined first in Bruno et al. (2018b). Sand Mitigation Measures (SMM) are essential in countering such adverse effects.

A recent and extensive review of SMMs is given in Bruno et al. (2018b) according to the new Source–Path–Receiver SMM categorization. It is inspired not only by the relative position of SMM to railway, but also by the SMM working principle and design goals, as sketched in Fig. 1(a). *Source SMMs* are directly located over sand sources (dunes or loose sand sheets), whatever is the spacing between them and the infrastructure. Their goal is to prevent erosion of sand from sand sources. Hence, their design and performances are fully independent from the type of infrastructure to be protected. Source SMMs include vegetated belts: km-wide green belts are by far wider than the railway corridor, and their objectives beyond the scope of the railway stakeholders; dozens meter-wide belts alongside line-like transport infrastructures (Wang et al., 1989; Dong et al., 2004) strongly depend on several physical, biological and economic factors. The most important ones are the quantity of available water and the costs of maintenance of the plants. For these reasons, vegetation-based SMMs have not been recently and explicitly permitted in recent design-and-build tenders for railways in hyper arid regions (Sobanski, 2018). *Path SMMs* are located along the windblown sand path ranging from the sand source to the infrastructure, at a safe distance from the latter. They are intended to promote sedimentation of the great bulk of incoming drifted sand, i.e. to significantly reduce the amount of sand reaching the infrastructure. Their overall design weakly depends on the kind of infrastructure to be protected, while their sand trapping performances are irrespective and independent of the local wind flow around the railway. *Receiver SMMs* are directly located on the infrastructure, e.g. the railroad or its shoulders. The above categorization clearly suggests a new rationale to the combined use of complementary SMMs, as programmatically stated in Bruno et al. (2018b), and previously raised by other authors (e.g. in Cheng and Xue, 2014; Xie et al., 2015; Cheng et al., 2016a,b). The ideal system follows from the contributions from individual SMM types, and results in a multi-layer protection. A highly efficient Path SMM stops the majority of the drifting sand, and provides manageable working conditions for a complementary Receiver SMM. The Receiver SMM can face the remaining low magnitude sand drift along the whole
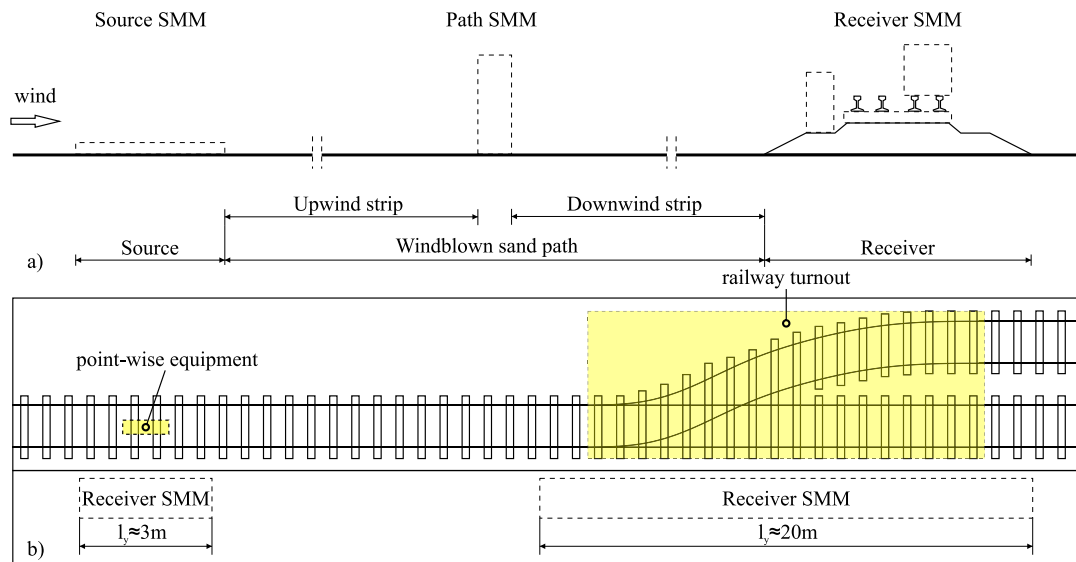
Fig. 1. Scheme of the multi-layer Source–Path–Receiver SMM protection (reprinted from (Bruno et al., 2018b) (a), plan view of point-wise Receiver SMMs along railway (b).

infrastructure, or secure point-wise sand-sensitive track components such as signalling devices or turnouts (Fig. 1-b).

The present study is limited to Receiver SMMs. Based on their working principle, they can be further divided in sand-resistant and aerodynamic-based Receiver SMMs.

Sand-resistant Receiver SMMs have been recently developed by modifying components of the track superstructure, in order to make them more resistant to the sand action, so to reduce its effects. Among them, let us recall ballastless track systems developed to cope with ballast contamination (e.g. Rheda 2000®slab track or Tubular-Track®in Merino, 2014; van der Merwe, 2013, respectively), ballast protection systems intended to mitigate its fouling (Keene et al., 2012; Dölçek, 2014) or its effects (Esmaeili et al., 2017), lubricant-free, grease-free, or hinge-free turnouts (Kóllmann, 2013), high-wear-resistance rail heads (Pointner et al., 2009; Kóllmann, 2013) and wheels (Faccoli et al., 2018). Interested readers can find more details in Bruno et al. (2018b).

Aerodynamic-based Receiver SMMs are intended to remove the sand action rather than just limiting its effects. Such a general goal is pursued by promoting wind-induced sand erosion from the railway and sand transport far from it. This SMM type is at its infancy: the few solutions proposed up to now are reviewed in Bruno et al. (2018b). In our opinion, there are three reasons for this delay: i. aerodynamic-based Receiver SMMs strongly interact with the railway substructure or the track components (e.g. rail, sleeper or slab, ballast) and depend on the railway functional requirements (e.g. rail gauge, safety distance from the track); ii. the aerodynamic behaviour of the railway substructure and superstructure is scarcely investigated in turn; iii. from the above mentioned, the partial rethinking of the conventional track systems is eventually due in order to improve their aerodynamic performances.

In the following, the study is focused on a single track system. Humped Sleepers (HS in the following) are selected because they are a prime example of the methodological issues mentioned above, and because of their specific prospective performances. HS elevate the rails by means of two rail chairs ('humps' in the following) at both ends of the sleepers resulting in a gap between the ballast surface, the rail foot and the side surfaces of two successive humps. HS have been brilliantly pioneered by Ramon-Rosales (1995) and Riessberger and Swanepoel (2005), further studied in Riessberger (2015) and Zakeri and Fathi (2017), and patented by Riessberger et al. (2014). The system has been tested by water channel tests (Ramon-Rosales, 1995), in situ observations along short segments of the Namibian (Riessberger

and Swanepoel, 2005) and of the Iranian (Zakeri, 2012) railways. Recently, Moyan et al. (2020) have proposed to make the gaps under the rails by removing portions of ballast between successive standard sleepers: even if such a proposal is almost equivalent in aerodynamic terms, it looks questionable with respect to the track mechanical behaviour. Analogously, humped slab tracks combine humps and ballastless systems (Zakeri et al., 2011). The qualitative reading of the air flow and sand sedimentation around HS is given in Bruno et al. (2018b), and graphically summarized in Fig. 2. The gap locally accelerates the airflow thanks to the well-known Venturi effect, locally induces high wall shear stresses, promotes sand erosion, and allows sand transport. Two potential critical issues result from the working principle: first, the air jetflow is expected to decelerate downwind the gap, potentially inducing sand sedimentation along the gauge; second, the Venturi effect is conjectured to weaken under yawed wind conditions because of the misalignment between the gap axis and the wind direction. The recent extensive computational campaign in Horvat et al. (2021) is aimed to fill the gap in the knowledge of the railway system aerodynamics and to quantify the potential advantages and disadvantages of the HS system. The study confirms that the track systems including elevated rails are the most promising solutions promoting sand erosion. Their performances are much higher compared to conventional ballasted track and ballastless continuous beam track (van der Merwe, 2013). However, the airflow deceleration along the gauge is confirmed for every incoming wind speed. It involves extensive sedimentation conditions at relatively low incoming wind speeds on most of the upper ballast surface. Sedimentation switches to windward or backward erosion at higher incoming wind speed, because the massively reversed flow induced by the ballast shoulder prevails over the weak jetflow induced by the gap. Yawed wind affects the HS performances to a minor extent, thanks to their cone-shaped geometry with rounded edges.

The present study aims at developing an innovative aerodynamic-based Receiver SMM called *Sand Blower*. It is intended to complement the HS track system and further improve its performances. The phenomenological knowledge gained in Horvat et al. (2021) paves the way to the heuristic conceptual design. The Computational Wind Engineering (CWE) approach allows the efficient sampling of the design space within the preliminary design. The detailed performance assessment of the retained design solution is compared to the standalone HS system adopted as a baseline.

The structure of the paper reflects the progression outlined above. Section 2 summarizes the wind flow modelling and adopted computational approach. Section 3 details the considered setups, in terms of
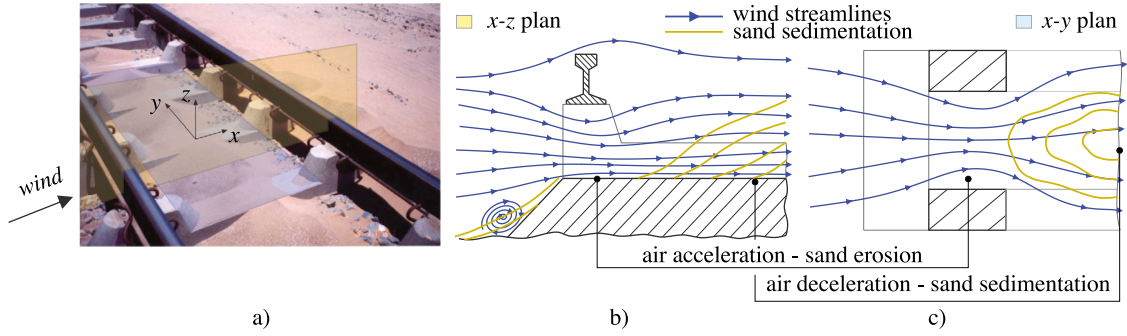
Fig. 2. Humped sleepers (reprinted from: Riessberger, 2015, a - with the permission to reuse under a Creative Commons Attribution License). Qualitative streamlines and sand accumulation levels in the plans $x - z$ (b) and $x - y$ (c) (redrawn from Bruno et al., 2018b).

incoming flow features and geometries of both the railway substructure and superstructure. The conceptual and preliminary design are critically discussed in Section 4. Finally, conclusions are outlined in Section 5.

2. Computational approach

In the light of the goals of the study, a flexible, relatively cheap but still accurate approach is mandatory in the conceptual design phase, in order to evaluate the performances of a huge number of design solutions. Two methodological remarks follow in such a perspective. First, the computational approach is preferred to Wind Tunnel (WT) tests, because manufacturing time and costs of the physical model are avoided, scaling issues do not affect the performance assessment (Raffaele et al., 2021), and a phenomenological sound reading of the aerodynamic effects induced by the SMM is made possible thanks to clear flow and shear stress visualization. Second, the full modelling of the multiphysics phenomena that induce windblown sand erosion, transport, sedimentation and avalanching are needed to fully describe the morphodynamics of the sedimented sand across the railway track: a body of literature exists about the modelling of the multiphase wind+sand flow in geomorphology and applied mathematics (see e.g. Zhang et al., 2012; Tsoar and Parteli, 2016; Lo Giudice et al., 2019) and in SMM specific applications (see e.g. Sarafrazi and Reza Talaee, 2019; Lo Giudice and Preziosi, 2020; Sarafrazi and Reza Talaee, 2020; Raffaele et al., 2022). However, air-only simulations are more adapted to the present study than air+sand multiphase ones, thanks to their relatively low computational cost, and because they are perfectly adapted to ascertain the working principle of the proposed aerodynamic-based SMMs.

Specific benchmarking between the adopted computational approach and previous experiments on railway embankment with track system and without rolling stock has not been carried out, because of the lack of publicly-available, high-quality, fully-described WT tests and related measurements of the local flow quantities relevant to the present application. However, the computational model adopted in the present study replicates in all its parts the one previously adopted in Horvat et al. (2021), and successfully fully validated in Bruno and Fransos (2015) against accurate, local wind tunnel measurements for the same class of aerodynamic problems and the same flow variables of interests. The class of problem is characterized by high-Re turbulent flow around a 3D bluff fundamental landform mounted on desert surface, dominated by boundary layer separation and reattachment. The comparison between WT and CWE results has been carried out in terms of local velocity field (see e.g. Figs. 9–10 in Bruno and Fransos, 2015, and accompanying comments) and shear stress distributions at ground (see e.g. Fig. 11 in Bruno and Fransos, 2015, and accompanying comments).

The main components of the CWE models are briefly summarized in the following: turbulence model and boundary conditions, numerical approach, computational domain, and spatial grid.

2.1. Mathematical model

The mathematical model adopted for the simulations of the high-Re, wall bounded turbulent flow belongs to the RANS approach. The approach is perfectly adapted to simulate the time-averaged flow features responsible for the long-term morphodynamics of sand dunes (e.g. in Liu et al., 2011; Araújo et al., 2013; Bruno and Fransos, 2015; Lima et al., 2017), and around railways (Zhang et al., 1995; Moyan et al., 2020). In particular, the Shear Stress Transport (SST) $k - \omega$ turbulence model is selected for the current application because of its proven accuracy in bluff-body aerodynamics in general (Menter, 1994; Menter et al., 2003), and for fundamental topographical forms (Bruno and Fransos, 2015), windblown sand solid barriers (Bruno et al., 2018a; Horvat et al., 2020), or railway embankments (Horvat et al., 2021). The whole set of governing equations in Einstein notation and Cartesian coordinates reads:

$$\frac{\partial \overline{u}_i}{\partial x_i} = 0, \tag{1}$$

$$\overline{u}_j \frac{\partial \overline{u}_i}{\partial x_j} = -\frac{1}{\rho} \frac{\partial \overline{p}}{\partial x_i} + \frac{\partial}{\partial x_j} \left[\left(\nu + \nu_t \right) \left(\frac{\partial \overline{u}_i}{\partial x_j} + \frac{\partial \overline{u}_j}{\partial x_i} \right) \right], \tag{2}$$

$$\overline{u}_j \frac{\partial k}{\partial x_j} = \frac{\partial}{\partial x_j} \left[\left(\sigma_k \nu_t + \nu \right) \frac{\partial k}{\partial x_j} \right] + \tilde{P}_k - \beta^* k \omega, \tag{3}$$

$$\overline{u}_j \frac{\partial \omega}{\partial x_j} = \frac{\partial}{\partial x_j} \left[\left(\sigma_\omega \nu_t + \nu \right) \frac{\partial \omega}{\partial x_j} \right] + C_{\omega_1} \frac{\omega}{k} P_k - C_{\omega_2} \omega^2$$
$$+ \left(1 - F_1 \right) \frac{2 \sigma_{\omega_2}}{\omega} \frac{\partial k}{\partial x_i} \frac{\partial \omega}{\partial x_i}, \tag{4}$$

where $\overline{u}_i$ is the averaged velocity, $\overline{p}$ the averaged pressure, ρ the air density, ν the air kinematic viscosity, k the turbulent kinetic energy, ω its specific dissipation rate, and ν_t the turbulent kinematic viscosity. The kinetic energy production term $\tilde{P}_k$ is modelled by introducing a limiter to prevent the build-up of turbulence in stagnation regions:

$$\tilde{P}_k = \min \left(P_k, 10\beta^* k \omega \right), \quad \text{where} \quad P_k \approx \nu_t \left(\frac{\partial \overline{u}_i}{\partial x_j} + \frac{\partial \overline{u}_j}{\partial x_i} \right) \frac{\partial \overline{u}_i}{\partial x_j}.$$

For the sake of conciseness, the definition of the blending function F_1 and the values of the model main constants β^*, σ_k, σ_ω, C_{ω_1} and C_{ω_2} are omitted herein. Interested readers can find them in Menter et al. (2003).

The SST $k - \omega$ model is complemented near the wall by the so-called sand-grain roughness wall functions. They are selected for the current application because of their wide use in environmental CWE in general (e.g. Blocken et al., 2007) and the proofs of adequacy obtained in previous 3D simulations of sand dune aerodynamics by Liu et al. (2011), Jackson et al. (2011, 2013), Bruno and Fransos (2015). In particular, standard wall functions (Launder and Spalding, 1974) with roughness modification (Cebeci and Bradshaw, 1977) are applied. The equivalent sand grain roughness height is determined as $K_s =$
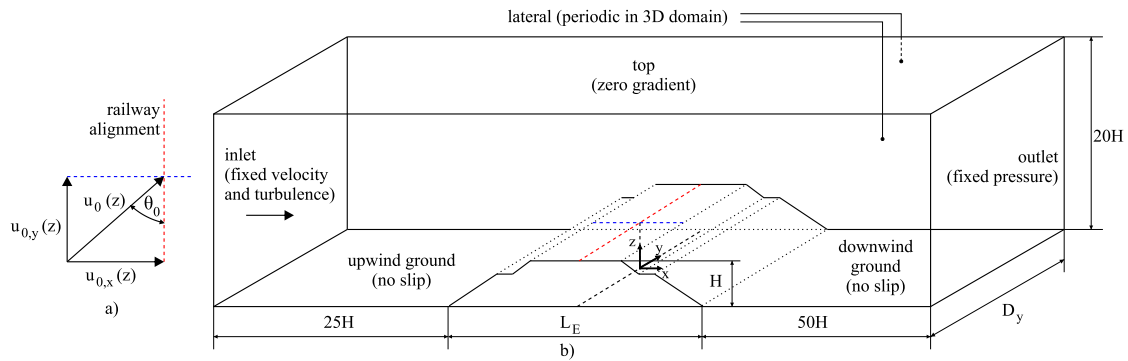
Fig. 3. Scheme of computational domain and boundary conditions (not in scale).

$9.793z_0/C_s$, where $C_s = 0.5$ is the roughness constant and z_0 is the aerodynamic roughness length.

The adopted computational domain is schematized in Fig. 3(b). Quasi-2D and 3D domains are adopted during the preliminary design and final performance assessment, respectively. Both domains include flat ground upwind and downwind the railway, and the railway substructure and superstructure. Some small-scale details of the track system and receiver SMM (e.g. fasteners) are not included for the sake of simplicity, being their expected effects on the overall flow negligible. The origin of the coordinate system is set at the far field ground level, positioned in a way that the $y - z$ vertical plane includes the railway longitudinal axis. The railway is arranged in the domain so that its longitudinal axis is normal to the domain lateral faces. The inlet, outlet, lateral, and top boundaries are placed at distances equal to or larger than the ones adopted in previous computational studies on analogous applications (e.g. Bruno and Fransos, 2015; Noguchi et al., 2019; Zhang et al., 2019), and by far large enough to avoid effects of boundary conditions (b.c.) on the results. The y-wise dimension of the domain is set equal to $D_y = 10H$ in 3D simulations, and to $D_y = 0.5H$ in quasi-2D ones, where H is the total height of the railway (Fig. 3-b).

No-slip b.c. is set at walls. Neumann zero-gradient b.c. is imposed for all the flow variables at the top and outlet faces, except for Dirichlet b.c. for pressure at outlet. Periodic b.c. are set at the lateral vertical faces in the 3D domains. The incoming upwind far-field is modelled by inlet b.c.: Neumann zero-gradient is used for pressure, while Dirichlet is imposed on u, k and ω. The profiles of $k_0(z)$ and $\omega_0(z)$ are set in accordance with (Richards and Norris, 2011) to replicate the neutral atmospheric boundary layer. The velocity profile is prescribed using the log-law $u_0(z) = \frac{u^*}{k} \log(\frac{z+z_0}{z_0})$, where $k = 0.41$ is the Von Kármán constant, u_* is the shear velocity, and z_0 is the aerodynamic roughness length. Such combination of velocity and turbulence is in equilibrium, ensuring that the specified profiles do not further develop in the domain. In order to account for yawed incoming wind-flow, the inlet velocity u_0 is split into the components $u_{0,x}(z) = u_0(z) \cdot sin(\theta_0)$ and $u_{0,y}(z) = u_0(z) \cdot cos(\theta_0)$, where θ_0 is the yaw angle with respect to the railway longitudinal axis y (Fig. 3-a). As extensively discussed in Horvat et al. (2021), the combination of the railway arrangement in the domain and adopted b.c. at inlet and side surfaces allows to keep the same spatial grid for any yaw angle, and to avoid tip effects at the end of the embankment.

2.2. Numerical approach

The space discretization is accomplished by a fully-structured grid consisting of hexahedral cells for both quasi-2D (see 4-a) and 3D cases (see 4-b). The following criteria have led the mesh generation and, in particular, its refinement around the ground and the railway: i. the geometry of the rail web and head is precisely discretized (Fig. 4-a) in order to accurately simulate the local flow around them. Bridging between different geometrical scales and related grid densities is a demanding goal, being the rail height up to about $1/74$ the substructure

height, i.e. about $1/6600$ the along-wind size of the whole domain; ii. the overall cell number is limited and related computational cost has to be affordable within the preliminary design; iii. the cell aspect ratio is kept lower or equal to 100, namely close to the ground and far from the railway; iv. the height n_w of the wall-adjacent cell provides a sufficiently-high mesh resolution in the normal direction n to the surface in order to adequately resolve the gradients of flow variables; v. n_w complies with the general wall function requirement so that cells adjacent to wall should be neither too thick nor too fine and their centre points lie in the logarithmic sublayer (in formulas $30 < n^+ = n_p u^*/\nu < 200$, where $n_p = n_w/2$ the cell centre height);); vi. n_w complies with the specific requirement of sand-grain roughness wall function so that grid cells have not their centre points within the physical roughness height (in formulas $n_p > K_S$). The adopted spatial grid with $n_w \approx 6$ mm is the finest one that satisfies both the n^+-based requirement involved by the wall function treatment ($100 < n^+ < 200$ for all the simulations), and the additional K_S-based requirement due for the sand-grain roughness wall function (n_p/K_S larger but close to unit for all the simulations). Hence, no significant further grid refinement at wall can be done within the adopted approach to wall treatment. About 40k cells are required to fully resolve the geometry in quasi-2D domains, while 13M cells are needed for 3D cases.

The Finite Volume open source code OpenFOAM© (Weller et al., 1998) is used to numerically evaluate the flow-field. The cell-centre values of the variables are interpolated at face locations using the second-order Central Difference Scheme for the diffusive terms. The convection terms are discretized by means of the so-called Limited Linear scheme, a second-order-accurate bounded Total Variational Diminishing (TVD) scheme resulting from the application of the Sweby limiter (Sweby, 1984) to the central differencing in order to enforce a monotonicity criterion. The SIMPLE algorithm is used for pressure–velocity coupling.

3. Problem setting

3.1. Incoming wind flow and sand features

The adopted incoming wind flow and sand features reflect common actual desert conditions.

The ground aerodynamic roughness length is set to $z_0 = 3e - 4$ m, according to the recommendations given in EN 1991-1-4 (2005). The incoming far-field wind shear velocity is set to $u_{*,0} = \sqrt{\tau_0/\rho} = 0.82$ m/s. Such a value is appropriately chosen in order to exceed the erosion threshold shear velocity u_{*t} for sand grain diameters in the range $d \in [0.063, 1.2]$ mm (Raffaele et al., 2016), i.e. windblown sand transport occurs upwind the railway. The resulting reference wind speed at the rail height equals $U_H = 13$ m/s, and the corresponding Reynolds number $Re_H = H \cdot U_H/\nu = \le 1.8e + 6$. Such value, together with the railway sharp-edged geometry, suggests that the flow is within the Reynolds super-critical regime, so that significant Reynolds effects are not expected to take place for any of the cases. To take into account
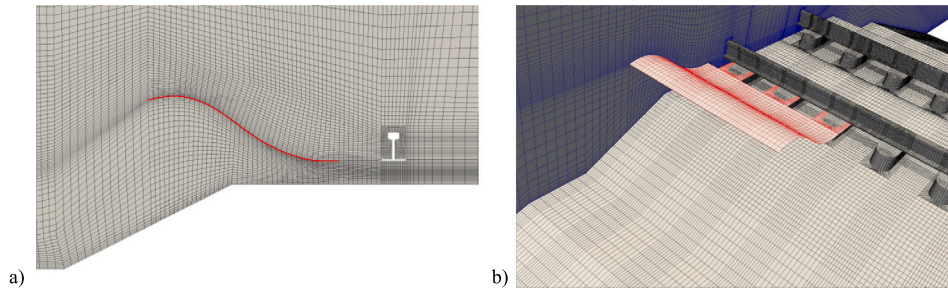
Fig. 4. Cross-section of the numerical mesh around of the Receiver SMM and the upwind rail (a); (b) Close up view of the 3D mesh around rails, humps, and Receiver SMM.
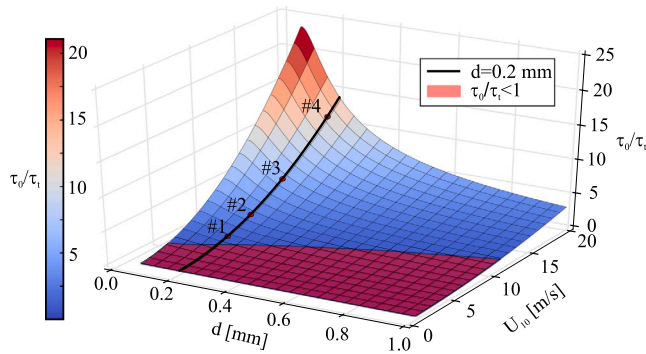

Fig. 5. Ratio τ_0/τ_t at the inlet boundary as a function of d and U_{10}.

incoming wind not perpendicular to the alignment, 3D simulations are carried out during the final performance assessment with yaw angles different than $\theta_0 = 90^\circ$. $\theta_0 = 75^\circ, 60^\circ, 45^\circ$ are adopted.

The adopted sand diameter d is equal to 0.2 mm, as the average value of diameters measured in general at the sites of interest (Horvat et al., 2021). The corresponding mean value of the erosion threshold shear stress is equal to $\tau_t = 0.09$ Pa (Raffaele et al., 2016).

The windblown sand erosion/sedimentation is mainly triggered by the ratio $|\tau|/\tau_t$, where $\tau(x, y, z)$ is the wind-induced local wall shear stress and $\tau_t(d)$ is the fluid threshold shear stress . Fig. 5 graphs the τ_0/τ_t ratio for varying the incoming wind velocity at 10 m height U_{10} and sand diameter. The surface above the isocontour $\tau_0/\tau_t = 1$ corresponds to the $U_{10} - d$ pairs that induce erosion. In order to discuss potential erosion/sedimentation patterns in different environmental conditions one can vary d and τ_t in turn, or equivalently U_{10} and τ_0 in turn. $d = 0.2$ mm is kept constant throughout the present study (thick black line in Fig. 5), while U_{10} is varied to sample four different wind classes in the Beaufort Scale (BS, red points in Fig. 5): #1-BS 4 moderate breeze, $\tau_0/\tau_t = 1.5$; #2-BS 5 fresh breeze, $\tau_0/\tau_t = 3$; #3-BS 6 strong breeze, $\tau_0/\tau_t = 6$; #4-BS 8 gale, $\tau_0/\tau_t = 12$. Within the given supercritical aerodynamic regime, the wind flow can be quantified by flow variables in dimensionless form because of the aerodynamic similarity, as it is done in many engineering areas, e.g. lift and drag coefficients. The dimensionless skin friction coefficient $C_f = 2|\tau|/\rho U_{10}^2$ is directly obtained from simulations. Later, the local ratio $|\tau|/\tau_t$ is obtained for the adopted instances of the Beaufort Scale by making C_f dimensional again with reference to the desired velocity: $\tau_{\#i}(x, y, z) = C_f(x, y, z)\frac{1}{2}\rho U_{10,\#i}^2$.

3.2. Baseline railway system

The whole railway system adopted in this study is schematized in Fig. 6. The letter L stands for horizontal dimensions, H for vertical dimensions, and AR denotes the slope aspect ratio. Subscript E refers to the embankment, B to the ballast and r to the rail. The railway substructure adopts standard low-rise embankment and ballast

bed commonly adopted in engineering practice. In particular, low-rise embankment is selected because it is a challenging benchmark for erosion-promoting receiver SMMs, being the wind speed at the rail level lower than for high embankments.

The adopted superstructure is the so-called Humped Sleeper track system (HS), inspired to the one patented by Riessberger et al. (2014). In the study, the height of the humps is equal to $H_H = 140$ mm. Standard 172 mm high Vignole UIC 60 rails are adopted. The standard gauge $L_g = 1435$ mm is adopted.

The total height of the railway system $H \approx 2$ m includes the embankment height H_E, the ballast height H_B, the height of the humps H_H, and the height of the rails H_r. Such a value is adopted as the aerodynamic reference scale in the following.

3.3. SMM conceptual design

The conceptual design of the proposed innovative Receiver SMM is carried out by an heuristic approach. It is grounded on the Authors' general knowledge about bluff-body aerodynamics, and on the specific knowledge in railway aerodynamics gained in Horvat et al. (2021), with particular reference to the performances of the HS track system.

The main features of the flow around the HS system are schematized in Fig. 7(a): the boundary layer (bl) separates at the ballast upwind edge and a separation bubble occurs; reattachment and flow speedup are induced by the gap beneath the upwind rail; a further bl separation results from the jet flow deceleration downwind the upwind rail, and from the massive reversed flow induced by the ballast bed and blown through the downwind gap. In short, HS performs locally well at the upwind rail, but conditions for sand sedimentation and backward erosion take place along the rest of the ballast upper surface (Horvat et al., 2021).

The proposed Receiver SMM is designed in the form of an S-shaped guide vane, as schematized in Fig. 7(b). Its purpose is to: i. drive the attacking flow, in order to suppress the bl separation and related bubble upwind the upwind rail; ii. increase the momentum across the upwind gap, in order to boost the jet flow along the whole gauge, and guarantee erosion conditions along it. Its Venturi-based working principle is expected to reach all the goals above: the vane leading edge catches the high-momentum flow from the upper part of the bl; the central part deflects the flow downwards; the trailing part directs the flow parallel to the upper ballast surface and towards the upwind gap. The conceived Receiver SMM is called *Sand Blower* (SB) because of its operating principle.

3.4. Preliminary design space

The parametrization of the SB geometry allows to define the preliminary design space. A generic shape of the vanes is referenced in Fig. 8(a). Relevant lengths of the track system are taken for reference from Fig. 6, i.e. the heights of the ballast H_B, of the gap H_H and of the rail H_r. The relative position of the SB leading and trailing edges with respect to the track system is defined by three design parameters, i.e. the horizontal distance of the leading edge from the ballast edge
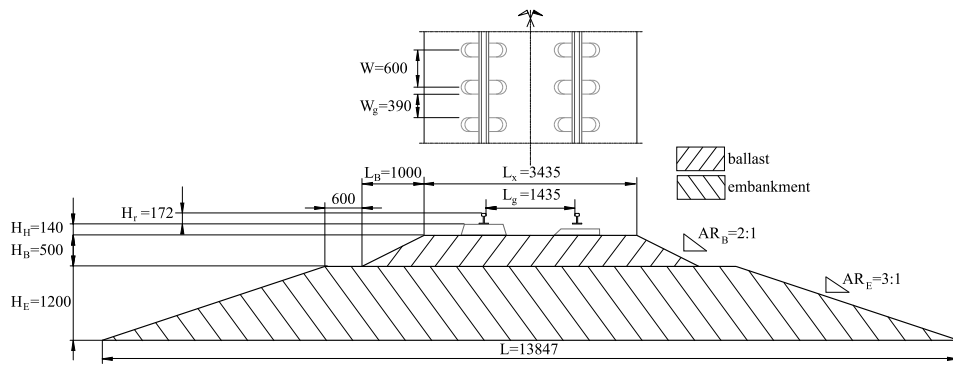
Fig. 6. Cross section and plan view of the baseline railway system (dimensions in mm).
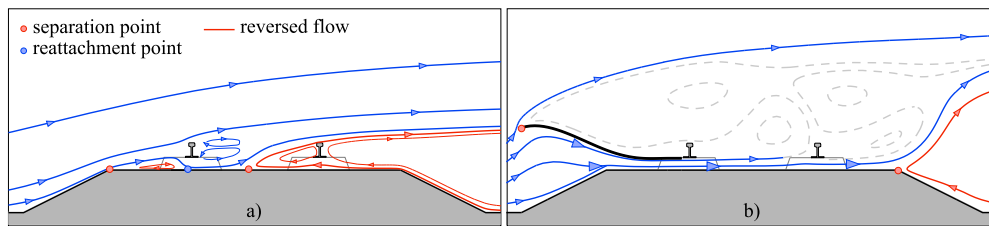

Fig. 7. Scheme of the simulated flow topology around HS track system (a, after Horvat et al., 2021), conjectured qualitative flow topology around the Sand Blower HS system (b, hardly predictable flow features in dashed grey lines). (For interpretation of the references to colour in this figure legend, the reader is referred to the web version of this article.)
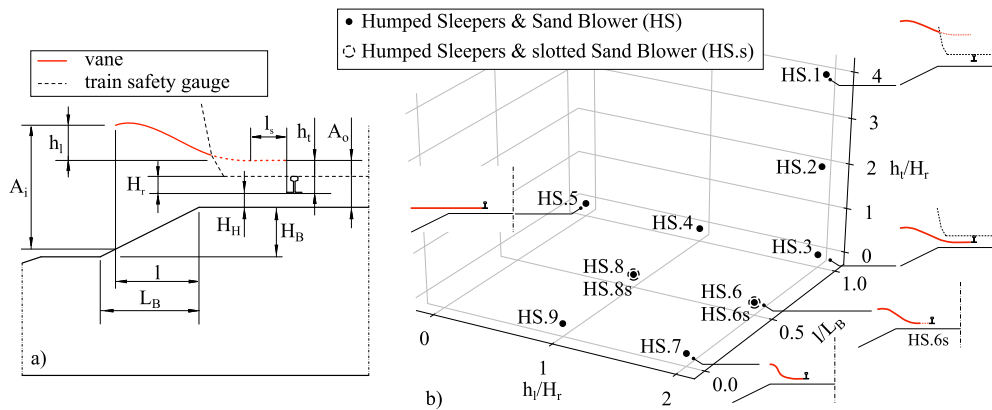

Fig. 8. Preliminary design space: alongwind cross section and main design parameters (a); sampled design space (b)

l, the vertical distance between the leading and trailing edges h_l, the height of the trailing edge from the rail foot h_t. Other SB geometrical features are set as constants: the trailing edge has the same x-coordinate of the upwind tip of the railway foot, and it has horizontal inclination, except in the cases where the vane intersects the safety gauge of the train; the leading edge is oriented along the direction of the local flow deflected upwards by the ballast shoulder, except in the limit case $h_l = 0$ (flat horizontal vane). The SB profile results from the above geometrical constraints.

The design parameters are made dimensionless with reference to the rail and the ballast height. The resulting three-dimensional design space is plotted in Fig. 8(b). It is explored by 9 samples, denoted as HS.i and marked with filled circles in Fig. 8 (b). The domain is systematically, but not fully sampled, because the exploration is addressed by a priori guidelines. Vanes from 1 to 3 are long, steep vanes placed at different heights: the higher the trailing edge, the steeper the slope at the trailing edge, because of the vane being cut by the train safety gauge. Vanes from 3 to 5 have the trailing edge at the height of the rail foot to avoid their intersection with the train safety gauge, and their overall height is progressively decreased up to the flat plate in HS.5. Analogously,

vanes 6, 7 and 8, 9 have horizontal length progressively shorter than vanes 3 and 4, respectively, in a cost-saving perspective. Finally, two additional vanes denoted with the letter 's' replicate HS.6 and HS.8 with a supplementary 250 mm wide slot between the trailing edge of the vane and the upwind foot of the rail. The slot is intended to allow the sand, which potentially sediments on the vane upper surface, to slip into the gap, and hence to be eroded by the accelerated flow underneath.

It should be noted that the joint effect of ballast bed and SB can be interpreted as an equivalent convergent duct that drives towards the rail both the upwards flow along the ballast side surface and the descending flow along the vane. Hence, the equivalent duct contraction ratio CR is a relevant although approximate bulk design parameter. CR is defined as the ratio of the areas at the inlet and outlet of the duct, expressed as $CR = A_i/A_o = (H_H + h_t + h_l + lH_B/L_B)/(H_H + h_t)$ (Fig. 8-a). For the considered samples CR ranges from 2 (HS.1) to 7 (HS.3). This being said, the effect of the vane is conjectured to prevail over the effect of the ballast shoulder, because of the high-momentum flow intercepted in upper part of the bl. Hence, the vane is expected to be effective for a ballastless humped slab as well (Horvat et al., 2021).
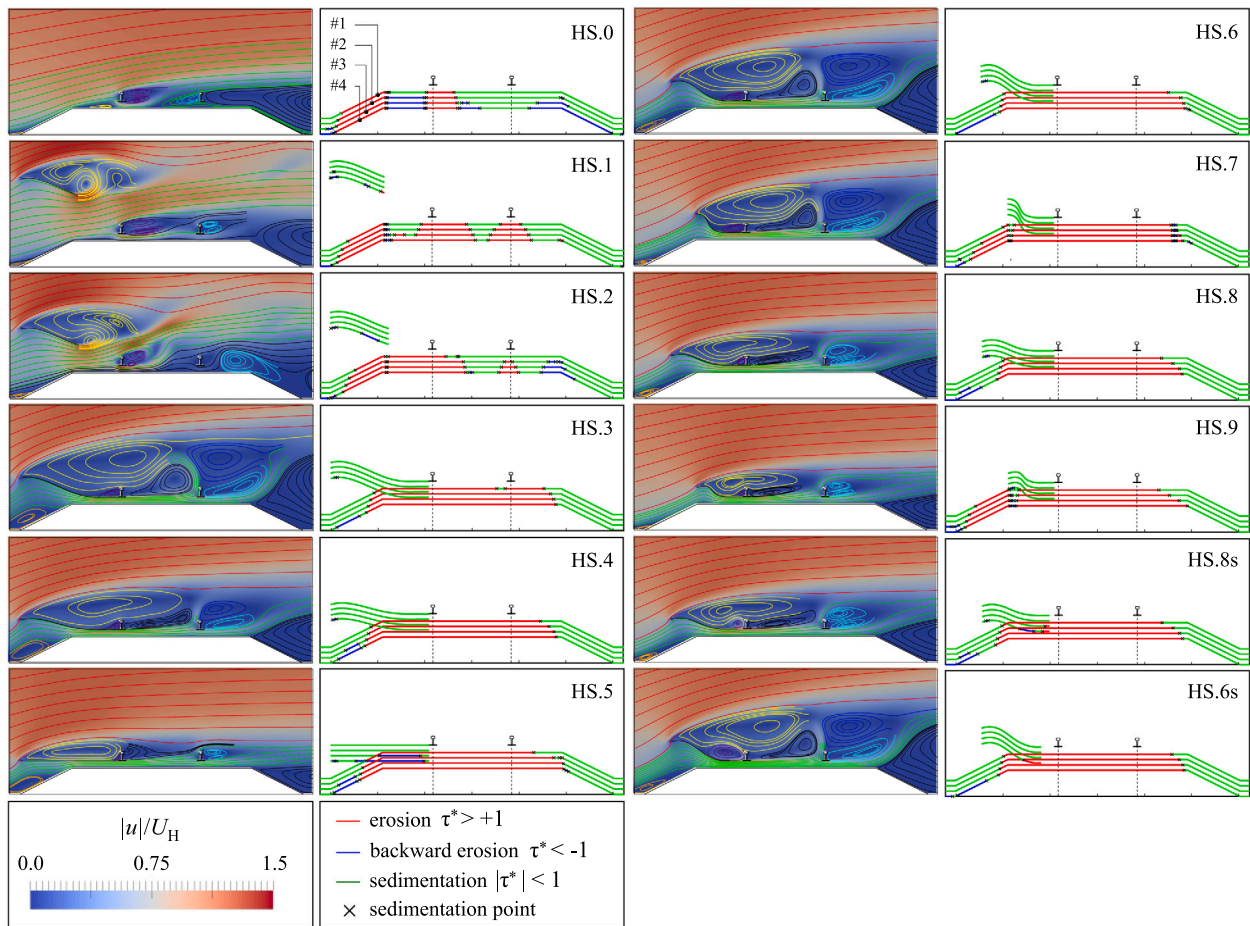
Fig. 9. Local flow patterns and potential sedimentation, erosion and backward erosion zones. (For interpretation of the references to colour in this figure legend, the reader is referred to the web version of this article.)

4. Results

4.1. Preliminary performance assessment

The preliminary performance assessment is intended to quantitatively test the samples of the design space. The study is carried out by quasi-2D simulations in order to approximate the flow by means of multiple cost-effective realizations. The quantitative preliminary performance assessment is based on the visualization of the flow topology, and on the map of wall shear stresses over the substructure and vane surfaces. In particular, the modified version of wall shear stresses $\tau^* = \frac{\tau_x}{|\tau_x|} \frac{|\tau|}{\tau_t}$ is defined to account for sand erosion and sedimentation. It is a dimensionless form which besides the magnitude, takes into account the direction with respect to the x-axis (see Fig. 3). Three characteristic conditions result: i. windward erosion (from now on simply called erosion, $\tau^* > 1$); ii. sedimentation ($1 > \tau^* > -1$); and iii. backward erosion ($\tau^* < -1$). The extent of the surface under erosion condition is a relevant performance metrics for a Receiver SMM such as the SB. Conversely, sedimentation and backwards erosion are conditions that potentially let the railway to attain SLS. In particular, backward erosion in the recirculation regions downwind the track is potentially hazardous, having the potential to transport back the sand from the downwind side towards the railway track.

Fig. 9 collects the flow fields and shear stress distributions above for the baseline unmitigated HS track system (HS.0), and for the eleven tentative design solutions. The field of the speedup ratio $|u|/|U_H$ is coupled with streamlines in the odd columns, while sedimentation, erosion and backward erosion (s.e.b.e.) zones are plotted in the even columns for the wind conditions #1, #2, #3, and #4 from top to bottom,

respectively. In general, with increase in the incoming wind speed (#1 to #4), and in τ_0/τ_t in turn, the erosion zones extend while sedimentation shrinks.

The s.e.b.e. mapping along the unmitigated HS reflects the flow structures already summarized in Fig. 7. The humped sleepers effectively promote sand erosion under the upwind rail. Conversely, the rest of the ballast upper surface lies in unintended sedimentation conditions for moderate breeze, and gradually migrate towards backward erosion for higher wind speed. Remarkably, the downwind gap is ineffective in promoting erosion even under gale conditions. Vanes having the trailing edge higher than the rail head ($h_t > H_r$, HS.1 and HS.2) do not provide optimal results from a practical point of view: the erosion condition extends, but significant sedimentation zones still hold for every wind speed. However, stimulating aerodynamic lessons can be learned from these cases. The vane completely changes the flow topology along the gauge. The vane-induced jet flow shows non-negligible speedup. However, the upwind rail acts as an unintended deflecting/blocking obstacle, and strongly affects the jet flow features and its effects that strongly depend on the vane level. In HS.1 the separation bubble is weakened, and the reversed flow along the rest of the ballast surface disappears, as testified by the vortex pair in the wake of both rails. In HS.2 the separation bubble is almost cancelled, but the jet flow around the upwind rail is strongly deflected upwards, the windward flow at the ballast level loses momentum, a clockwise vortex follows around the ballast trailing edge, and backward erosion takes place in turn. A decisive improvement is accomplished by moving the vane to the level of the rail foot. All the corresponding cases ($h_v = 0$; from HS.3 to HS.6s) have the same qualitative flow topology. The bl no longer separates at the ballast leading edge. The two counter rotating vortices in the
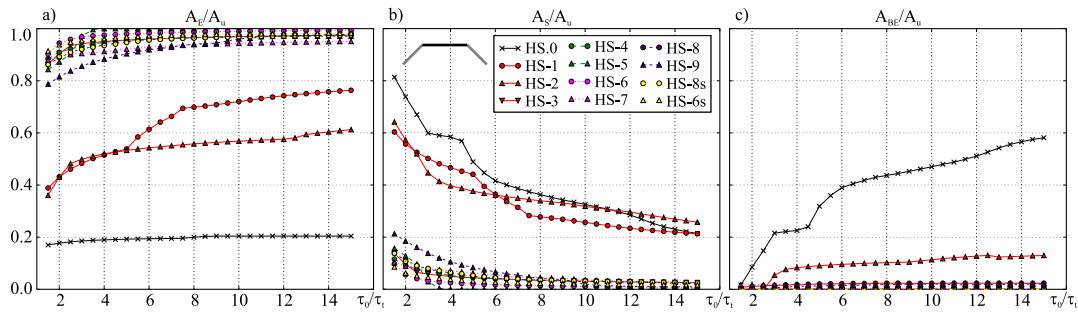
Fig. 10. Erosion (a, A_E), sedimentation (b, A_S), and backward erosion (c, A_{BE}) on the upper ballast surface A_u.

vane wake (HS.1 and HS.2) are replaced by a single, larger recirculation region (yellow streamlines) accompanied by a small secondary vortex just in front of the upwind rail (purple). The vane-induced jet flow fully blows along the upwind gap, and to a minor extent also along the downwind one. A single counterclockwise recirculation occurs along the gauge (black), and a pair of counter rotating vortices downwind the downwind rail (blue and light blue). The speedup ratio fields reveal that all the flow structures in the wake of the vane (yellow, black, blue, and light blue) and in the ballast wake have very low momentum ($|u|/U_H \leq 0.1$). In average terms, the overall flow is characterized by a strong shear layer at the top and a high-speed jet at the bottom, together with a nearly stagnant wake in between. The flow features close to the ballast bed secure full erosion conditions for the very most of its horizontal surface, and under all wind conditions. Conversely, the low energy wake of the vane implies that its upper surface is prone to sedimentation in all configurations. Further explorations from HS.3 are intended to reduce the size of the vane while keeping the same performance in a cost-saving perspective. Low-rise vanes (HS.4, HS.5) have erosion performance analogous to HS.3. The shortest tested vanes (H.7, HS.9) suffer a small sedimentation zone at the upwind sharp edge of the ballast, due to the insufficient squeezing of the bl. These solutions are not investigated further to avoid possible obstruction of the vane by sedimented sand or other windblown debris. Moderate shortening (HS.6 and HS.8, with vane leading edge corresponding to the mid-point of the ballast upwind shoulder) does not cause risk of the rail obstruction. In the same time, it shows performance comparable to the longer vane (HS.3) and significantly reduces construction costs. By taking the above into account, two additional simulations are carried out on slotted HS.6s and HS.8s. The slot does not involve significant aerodynamic effects, except for the size of the secondary vortex (purple) between the vane and the rail upwind face. Prevailing sedimentation conditions still hold along the vane upper surface, except around the trailing edge under gale conditions. Nevertheless, the slope angle in HS.6s is greater than the dry sand angle of repose ($\approx 30°$). This lets the sedimented sand to avalanche through the slot into the eroded gap, and the vane upper surface gets passively cleaned.

The concise assessment of the SB behaviour is given in Fig. 10 by means of three dimensionless bulk quantities. A_E, A_S, A_{BE} result from the integral of the erosion, sedimentation, and backward erosion areas over the ballast upper surface, respectively. They are rescaled by the total area of the surface A_u. It follows that each metric can vary in the range [0:1], and that $(A_E + A_S + A_{BE})/A_u = 1$. A_E/A_u is a proper performance metric for aerodynamic-based Receiver SMMs, and for the Sand Blower in particular. Conversely, the higher A_S and A_{BE}, the lower the performance of SB. The range of the incoming velocities from BS4 to BS8 is densely sampled. The resulting interval of the stress ratio $1.5 \leq \tau_0/\tau_t \leq 12$ is sampled with a step $\Delta_\tau = 0.5$. The trends of these metrics versus τ_0/τ_t reflect what is previously commented. The higher τ_0/τ_t, the lower the sedimentation and the higher the erosion/backward erosion. The clustering of the curves points out three subsets of design solutions. The unmitigated case (HS.0) shows non-negligible, but relatively low performance in erosion, decreasing sedimentation, and
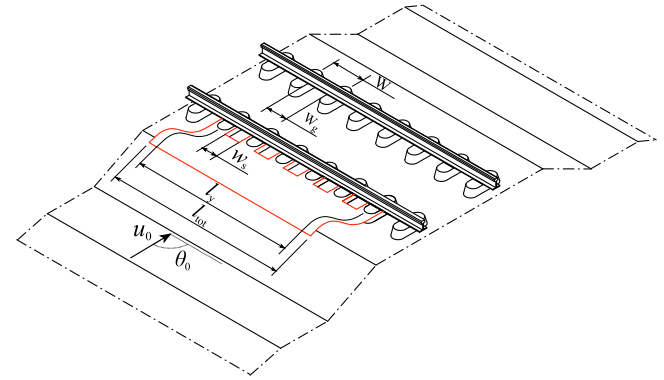

Fig. 11. SB 3D geometry.

increasing backwards erosion versus τ_0/τ_t. The cases with the highest vanes (HS.1, HS.2) show similar sedimentation trends compared to the unmitigated case. HS.1 and HS.2 have significantly improved overall erosion performance at lower wind speed because the flow is not reversed. At higher wind speed HS.2 suffers a loss of performance because the reversed flow at the ballast trailing edge gains momentum and induces backward erosion. All the cases with the vane trailing edge at the level of the rail foot ($h_v = 0$, from HS.3 to HS.9) show the best overall performances: erosion extends over the most of the ballast upper surface ($0.8 \leq A_E/A_u \leq 1$), backwards erosion is negligible under every tested wind condition, and sedimentation nearly vanishes for $\tau_0/\tau_t > 5$. In particular, the design solutions HS.6 and HS.6s are the most promising, thanks to the high and nearly constant erosion performance. The remaining differences in the performance level of this subset are difficult to be commented in detail since their magnitude is smaller than the expected numerical error coming from the intrinsic features of 2D simulations.

In the light of the above, the design solution HS6.s is selected for further development. In the following, we refer to HS.6s as 'Sand Blower' (SB), and to HS.0 as 'Humped Sleepers' (HS) for the sake of conciseness.

4.2. Enhanced performance assessment under orthogonal wind

The enhanced performance assessment is carried out by 3D simulations. The corresponding geometry of HS and SB are shown in Fig. 11. The adopted track-wise length $l_y = 3$ m corresponds to 5 sizes of the hump spacing W. However, l_y can be adapted to the protected equipment, as exemplified in Fig. 1(b). The vane is fixed at the upwind rail and humps by rail fasteners. The track-wise length of the slot w_s is set to 310 mm. At the stage of preliminary design, a simplified SB is studied: the components which are essential from the structural point of view, but have expected negligible aerodynamic effects, are not included in the simulations (e.g. vertical stiffening baffles at the vane lower surface).
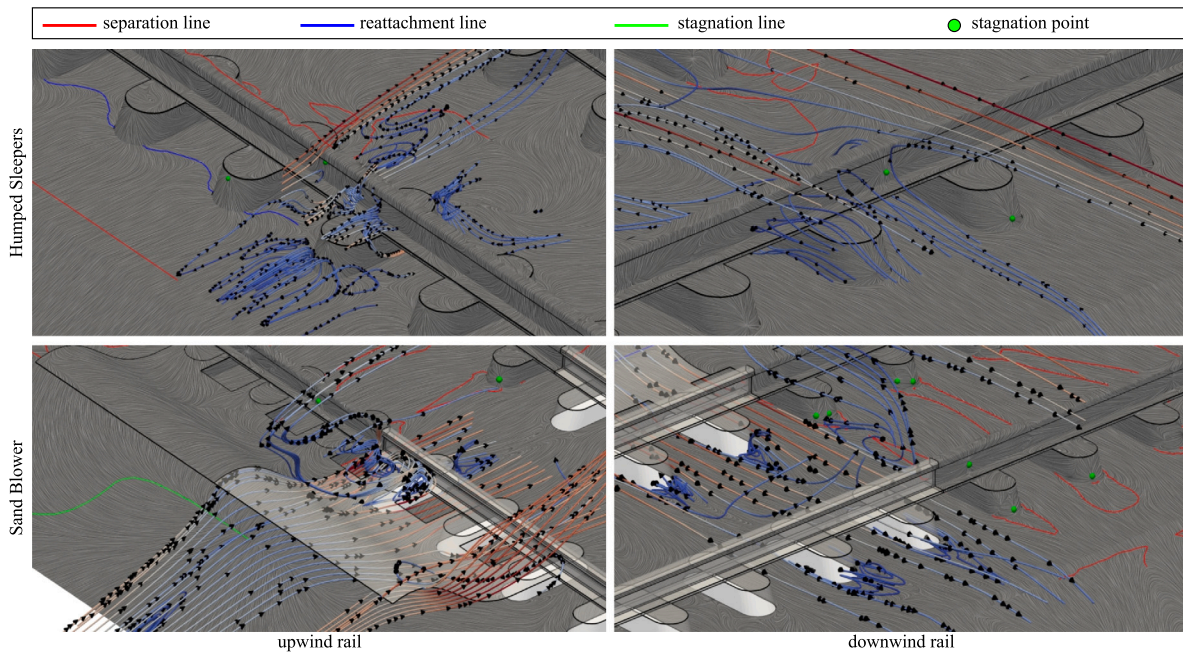
Fig. 12. Flow patterns around unmitigated HS and SB cases (orthogonal incoming wind from left to right).

At the first stage, only orthogonal wind velocity is considered ($\theta_0 = 90°$). Fig. 12 plots the streamlines of the local flow around the Sand Blower, and compares it to the unmitigated HS baseline case. To make the figure clearer, the flow visualization is presented from two point of views: the upwind rail (left column) and the downwind rail (right column). Each visualization field is further split in half by the median alongwind vertical plane ($x - z$ plane). The right half is dedicated to streamlines, while the left side to selected separation, reattachment, and stagnation lines and points obtained from the τ field. The flow direction at solid walls is visualized by means of the *Line Integral Convolution* (LIC, Cabral and Leedom, 1993) applied to the τ vector field. If the condition for sand erosion is satisfied $|\tau^*| > 1$, the direction of the erosion is locally parallel to the LIC lines. The 3D flow around HS has already been thoroughly discussed in Horvat et al. (2021). It is summarized here for reference: the flow is accelerated under the upwind hump; the part of the flow entering the gaps follows their geometry, and it separates in the middle of the gauge because of the reversed flow blowing through the downwind gaps. The qualitative features of the flow predicted by the 2D simulations are confirmed. However the 3D structures which occur at the gaps and in the wake of the humps are expected to have significant effects on the s.e.b.e. patterns. The flow structures change when SB is applied to HS. The majority of the flow is accelerated under the upwind rail and enters the gauge without the recirculation zone that occurs upwind the humps in the HS case. A small fraction of the flow escapes through the slot and is dragged into the recirculation zone downwind the vane. At the joints of the upwind rail and the Sand Blower, pairs of counter-rotating vertical-axis vortices occur. Classical alongwind swirling takes place at the track-wise tips of the Sand Blower, caused by the pressure difference between the upper and lower surfaces. The 3D simulation confirms the overall excellent aerodynamic behaviour observed in the 2D cases. The accelerated flow remains attached to the upper ballast surface and leaves the gauge under the downwind rail thanks to the suppression of the reversed flow. Only a small fraction of the flow crosses over the downwind rail, because of the lift effect of the humps. Additionally, in the wake of each hump, an arch vortex takes place.

Fig. 13 details the vertical and horizontal profile of the velocity at the upwind and downwind gaps (Fig. 13-a and -c, respectively), and in the mid of the gauge (Fig. 13-b). The speedup induced by the Sand Blower is evident. At the upwind gap, the x-speed increases from $u_x/|u_0| \approx 0.5$ (HS case) to $u_x/|u_0| \approx 0.9$ (SB case). At mid-gauge the effects are even more striking: the nearly stagnant flow in the HS case gains momentum in the SB case ($u_x/|u_0| \approx +0.8$). An analogous effect takes place at the downwind edge: the reversed flow observed in the HS case ($u_x/|u_0| \approx -0.2$) has the opposite direction in the SB case ($u_x/|u_0| \approx +0.5$).

The 3D flow fields described above deeply impact the s.e.b.e. patterns around the railway track surface. They are shown in Fig. 14 in plan view. The comparative analysis of the HS and SB performances develops through four specific points.

First, under *moderate breeze conditions* (#1), the HS system performs as expected across the upwind gap where erosion conditions take place. Conversely, most of the remaining upper ballast surface lies in the sedimentation condition, including the downwind gap. Under the same incoming speed, the SB enforces erosion conditions along the whole upwind horizontal ballast surface. Most importantly, SB secures continuous erosion and windward transport across the gauge. Sedimentation condition holds where interaction with the humps blocks or lowers jet flow momentum, e.g. the narrow along-wind stripes aligned with the humps, and the downwind horizontal ballast surface.

Second, for HS under *stronger incoming winds* (#2 to #4), the erosion condition under the upwind hump slightly extends into the gauge. Most of the sedimentation area turns into backward erosion because of the bl separation downwind the upwind ballast edge and the massive, reversed flow along the ballast downwind slope, that extends into the gauge through the downwind gaps. The combined effects of erosion at the upwind gap and backward erosion at the downwind gap is expected to move the sand from the both rails and to pile it up at the middle of the gauge, as confirmed by the field observations (Riessberger, 2015, Fig. 2-a). Such an occurrence partially defeats the purpose of ballasted Humped Sleepers which are designed to keep the gauge sand-free. Under the same wind conditions, the Sand Blower ensures supplementary erosion along the downwind horizontal surface of the ballast. In such a way, the alongwind sand transport path is secured along the whole horizontal ballast surface. Conversely, SB is unable to further significantly shrink the alongwind stripes between humps, where backward erosion progressively replaces sedimentation.

Third, SB causes an unintended effect along the *upwind ballast shoulder*, where sedimentation is induced at low wind speed, and backwards
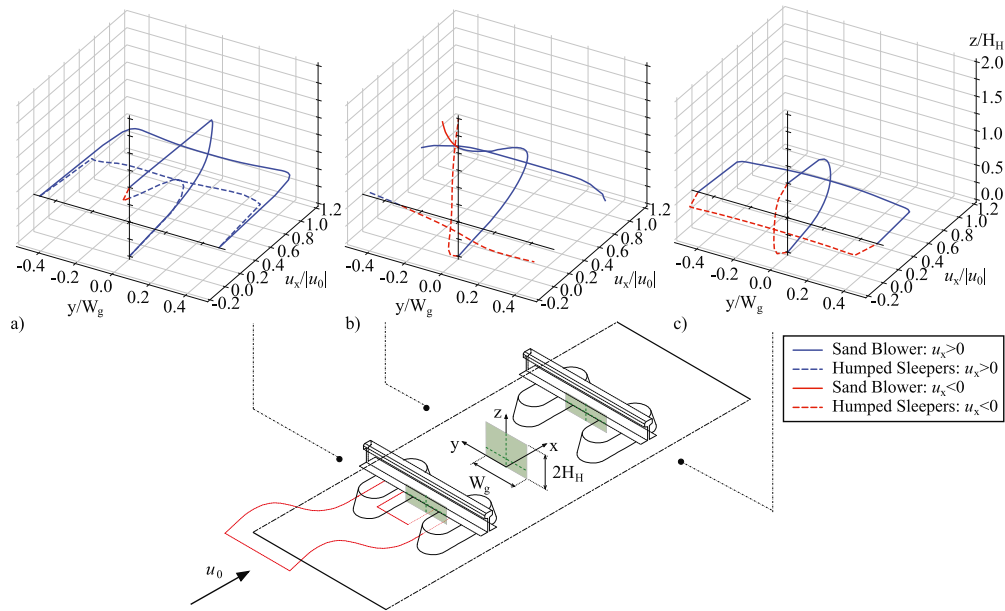
Fig. 13. Spanwise and vertical profiles of the local wind x−velocity across the upwind gap (a), the gauge (b), and the downwind gap (c) .
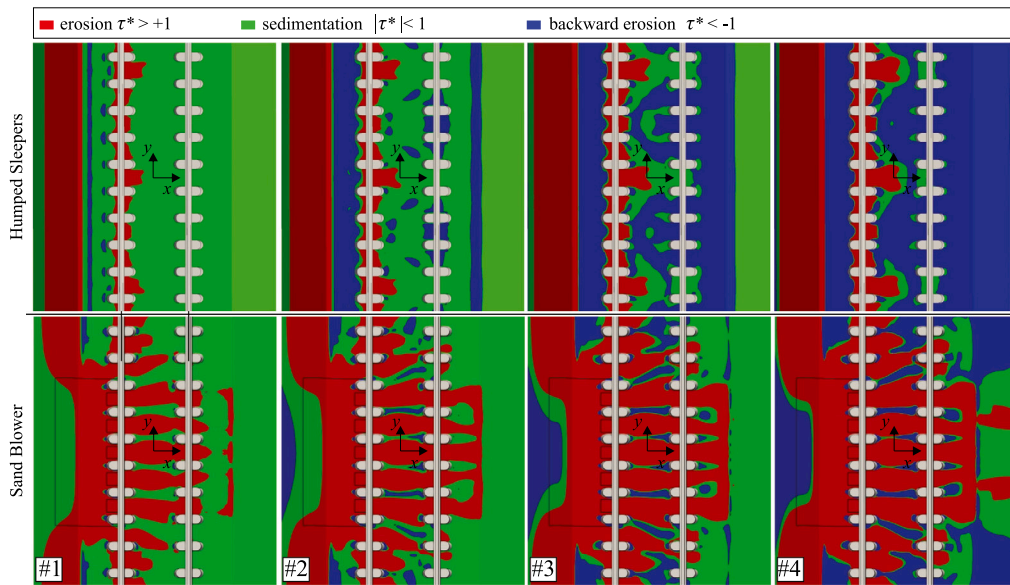

Fig. 14. Potential s.e.b.e. patterns for unmitigated HS and SB cases (incoming orthogonal wind from left to right).

erosion under gale conditions. Here, the vane-free ballast bed locally performs better, with the erosion condition satisfied for all of the tested incoming winds.

Finally, the SB vane also affects the flow along the *track-wise direction*. On the one hand, the s.e.b.e. patterns repeat periodically with the same spacing of the humps, while the track-wise wavelength of the patterns in HS equals four times the hump spacing (Horvat et al., 2021). On the other hand, as expected, transition s.e.b.e. patterns occur at the free ends of the vane along a couple of humps, because of the tip swirling vortices.

The performance metric A_E/A_u of Humped Sleepers and Sand Blower obtained from 2D and 3D simulations are compared in Fig. 15. The complementary bulk metrics A_S/A_u and A_{BE}/A_u are plotted as well. The 3D simulations confirm good overall performances of the Sand Blower with respect to the unmitigated Humped Sleepers. SB more than quadruples the erosion performance of the HS system for any wind speed. Consequently, SB drastically reduces the sedimentation at the

low and moderate wind speeds ($\tau_0/\tau_t < 10$), and backward erosion for any values of τ_0/τ_t. In general, the differences between the 2D and 3D simulations are due to the track wise varying geometry. This causes the changes in the flow structures, and inevitably different s.e.b.e. patterns. SB erosion performance decreases by about 10% from 2D to 3D, induced by the growth of sedimentation and backward erosion versus τ_0/τ_t. The HS show almost constant erosion performance versus τ_0/τ_t, nearly equally predicted by both the 2D and 3D simulations. However, this does not mean the overall flow is 2D: erosion conditions take place upwind the upwind rail only, where the flow is almost track-wise constant. Downwind from it, the 3D features are more prominent than in the SB case, but they merely result in a progressive switch between sedimentation and backward erosion conditions. In short, the comparison confirms a-posteriori that 2D low fidelity and cheap models return acceptable qualitative trends within an extensive sensitivity analysis, but that 3D simulations are mandatory to properly account for the intrinsically 3D periodic geometry of the track system.
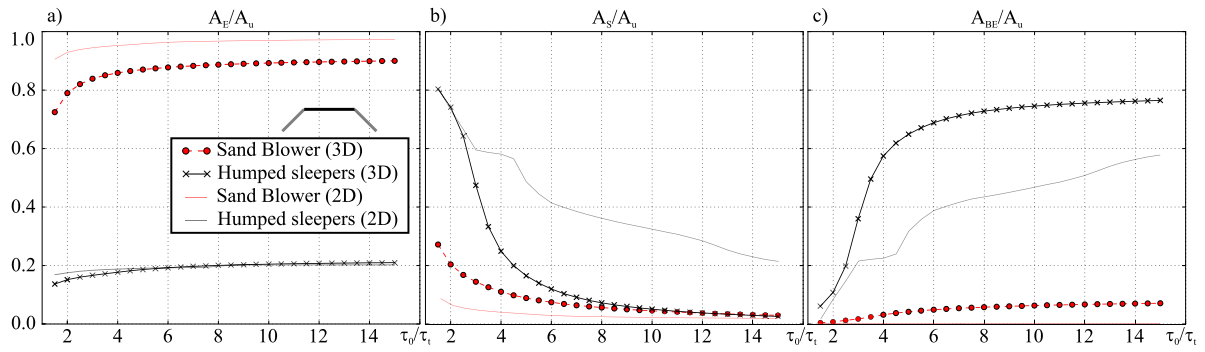
Fig. 15. Erosion (a), sedimentation (b), and backward erosion (c) normalized areas for HS and SB from 2D and 3D simulations.
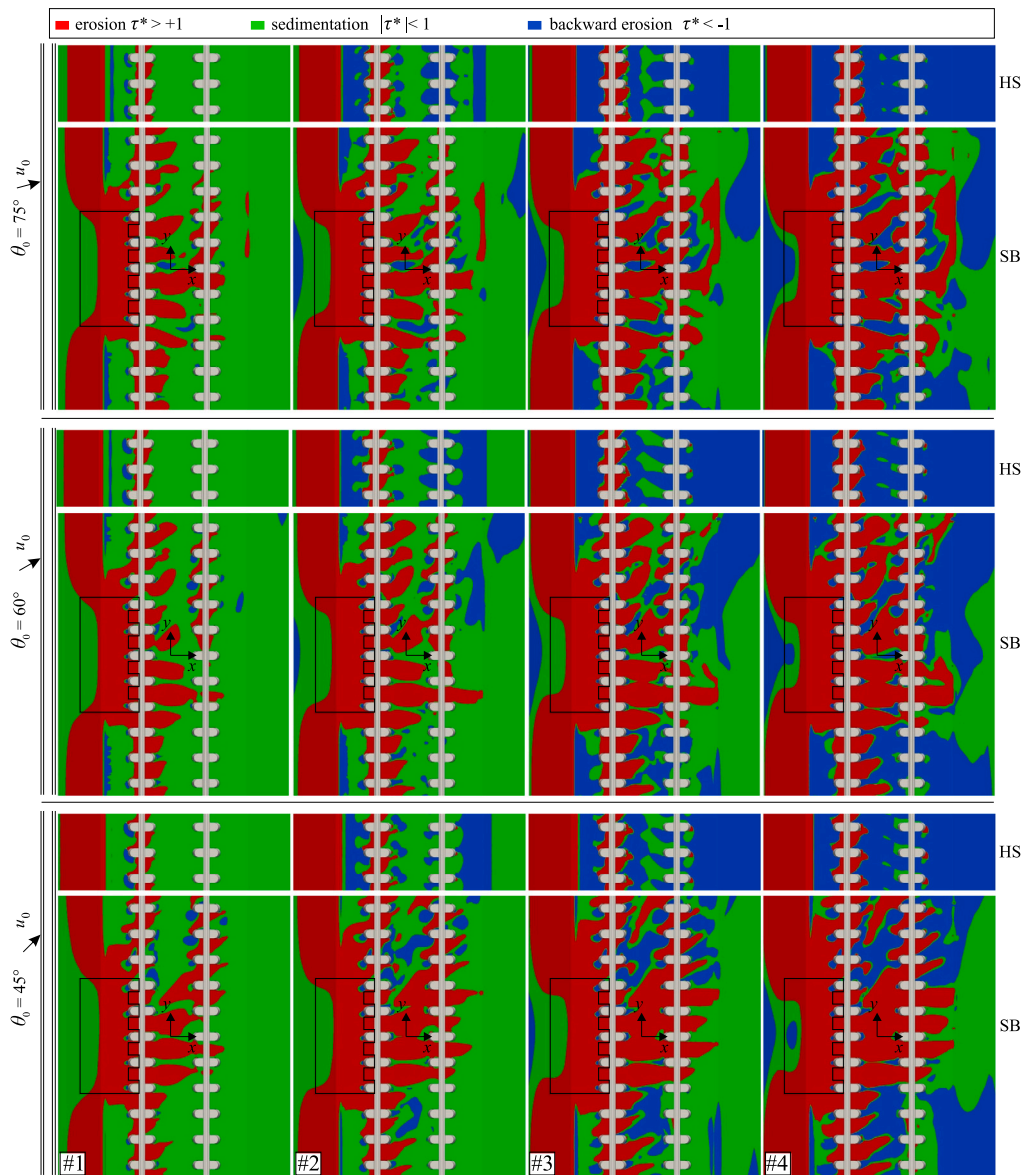

Fig. 16. Potential s.e.b.e. patterns for unmitigated HS and SB cases at different yaw angles (incoming wind from left to right).

4.3. Enhanced performance assessment under yawed winds

In order to investigate the effects of yawed wind, $\theta_0 = 75°$, $60°$, and $45°$ have been simulated for both the Humped Sleepers and Sand Blower. Fig. 16 shows the s.e.b.e. patterns in plan view for the selected

yaw angles and incoming wind speeds. Two main remarks are outlined for the sake of conciseness.

In trackwise average, the erosion zones under the upwind rail in the HS track under skewed winds are reduced in size and more skewed compared to those under the orthogonal wind. Moreover, the more
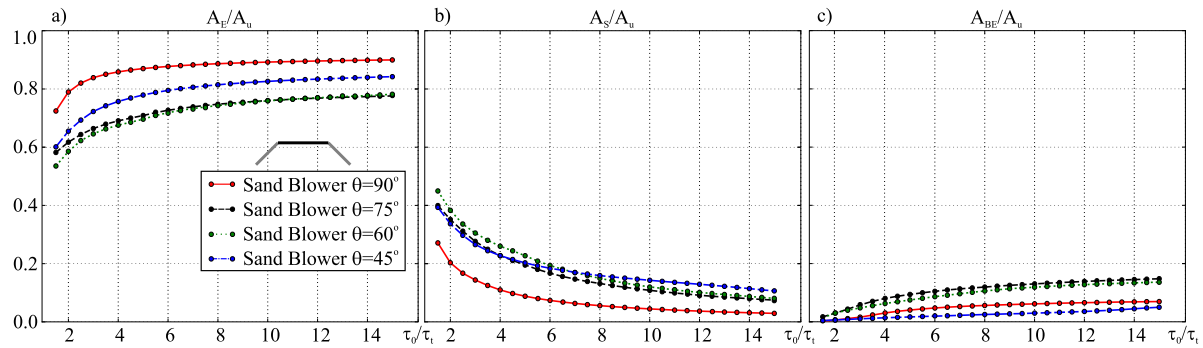
Fig. 17. SB case: Trackwise averaged values of erosion (a), sedimentation (b), and backward erosion (c) normalized areas at different yaw angles.

yawed the wind, the larger and more skewed the backward erosion zone in front of the upwind humps. Such evidences reflect the massive flow separation around the upwind hump, that subtracts momentum from the jetflow through the upwind gap. The SB secures continuous erosion patterns along the gauge also under skewed winds. Moreover, the backward erosion zone in front of the upwind humps is very small, and nearly insensitive to the wind yaw angle and speed. These patterns occur because the SB inhibits massive flow separation at the upwind humps under yawed winds, and ensures that the humps act as additional guiding vanes that drive the flow along the gaps.

Trackwise variability of the s.e.b.e. patterns around the SB under yawed winds is higher than under orthogonal wind. In particular, the erosion patterns along the gauge at the trackwise position of the SB tips are no longer continuous and are deflected from the gap axis under low speeds (#1 and #2). These local features result from the effects of the yaw angle on the tip swirling vortices. It is expected that a longer SB preserves the overall periodic s.e.b.e patterns along its central segment.

The performance bulk metric A_E/A_u of the Sand Blower under yawed winds is plotted in Fig. 17(a), together with the complementary metrics A_S/A_u and A_{BE}/A_u in Figs. 17 (b) and (c), respectively. The averaging is performed along the whole track-wise dimension of Sand Blower ($A_u = L_x l_{tot}$). Overall, the SB performances under yawed winds are lower than the ones under orthogonal wind. Nevertheless, they still remain by far higher compared to the HS. Both sedimentation and backward erosion increase in the face of the smaller sedimentation area. Interestingly, the trend of the bulk metrics is not monotonic versus the yaw angle: the minimum performance occurs for nearly all the wind speeds at about $60° \leq \theta_0 \leq 75°$. Under extremely yawed wind ($\theta_0 = 45°$) the erosion recovers and approaches the values of orthogonal wind, while backward erosion attains its minimum. On the one hand, such non trivial trends reflect the intricate, highly 3D flow, where local bl separation and reattachment phenomena can affect the global s.e.b.e. patterns. On the other hand, they result from the trackwise averaging of the heterogeneous s.e.b.e. patterns. In order to evaluate the trackwise variability induced by the SB free ends the performance bulk metric A_E/A_u is evaluated for each gap p_i ($i = 1, 4$) in Fig. 18 ($A_u = L_x W$). The performance of each gap is compared with the values of the whole track-wise average under perpendicular wind. Two main remarks follow. First, one of the two end gaps alternatively suffers the lowest local performance under a given yawed wind (p_1 for $\theta_0 = 75°$ and 45°, p_4 for $\theta_0 = 60°$). We conjecture this depends on the swirling tip vortex that negatively affects, to the major extent, the shear stresses at the ballast surface. Second, the best performances are often obtained at the central gaps (e.g. p_2 for $\theta_0 = 75°$ and 45°), but not necessarily (e.g. p_1 for $\theta_0 = 60°$). In short, in spite of the short SB, 1 out of 4 gaps performs similarly to the SB under perpendicular wind. The remaining gaps suffer a performance drop up to about 20%.

5. Conclusions

In this study, the semi-heuristic conceptual design of a new Receiver Sand Mitigation Measure has been developed on the basis of the detailed knowledge of the aerodynamic behaviour of the baseline railway track system. The sampling of the design space and the performance assessment have been carried out by different computational models adapted to the design stages covered in the study. Three final remarks can be outlined:

- the unmitigated Humped Sleeper track system performs well at the upwind rail with respect to standard track systems, but the mid-gauge flow separation induces undesired sedimentation and backward erosion at the downwind rail, trapping the sand in between the gauge. It follows that only the 20% of the overall ballast surface is subjected to natural erosion;
- the Sand Blower coupled with Humped Sleepers increases by 450% the ballast surface subjected to natural erosion compared to Humped sleepers only under a wide range of incoming orthogonal wind speeds ($2 \leq U_{10} \leq 20$ m/s). The boundary layer is forced to remain attached to the ballast surface, and the jetflow along both gaps and across the gauge significantly gains momentum. A continuous sand erosion and transport path is secured along the whole railway track;
- the Sand Blower performs well under a wide range of yaw angles ($45° \leq \theta_0 \leq 90°$): the ballast surface subjected to natural erosion is reduced in average by no more than 11% compared to orthogonal winds. However, significant local tip effects take place. Having this in mind, SB trackwise length longer than the railway segment or point-wise equipment to be protected is of outmost importance in real world working conditions.

In short, Sand Blower in combination with Humped Sleepers appears as a promising design solution from the industrial point of view, thanks to its low cost, ease of construction, high efficiency, aerodynamic robustness, and flexible deployability to protect pointwise railway components against massive sand flux, or to protect the whole railway segment facing to moderate incoming sand drift.

The conceptual and preliminary design pave the way to the further design stages: computationally-based aerodynamic optimization (Horvat et al., 2020) of the Sand Blower shape intended to maximize its performances and to minimize the tips effects under yawed winds; as-built design, intended to make the Sand Blower compliant to construction requirements, and to railway maintenance; final performance assessment towards technical qualification of the technology by means of experimental tests. Two-phase wind tunnel tests on a scaled model are difficult to implement because of the different characteristic lengths of the railway substructure, the track system, the Sand Blower and the sand grains, and the resulting lack of similarity requirements (Raffaele et al., 2021). Even if a hybrid approach coupling computational and wind tunnel tests (Raffaele et al., 2022) is a promising future perspective, full-scale field tests remain at the time being the most suited
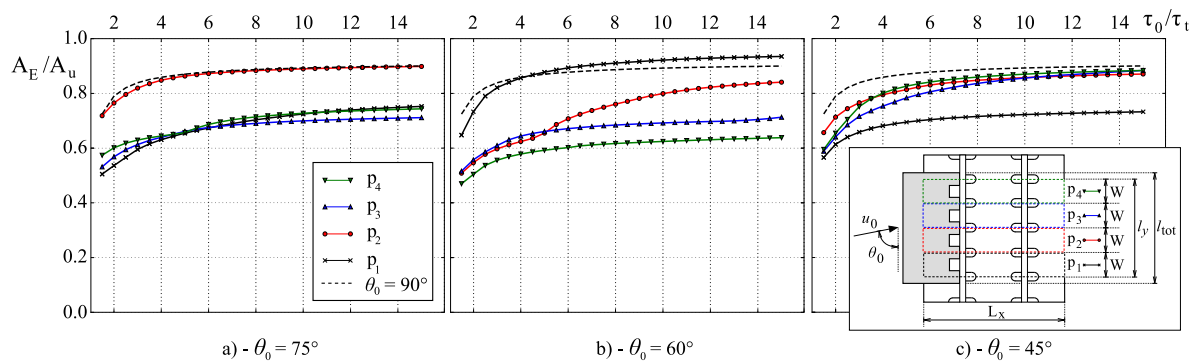
Fig. 18. Local erosion normalized areas for gaps 1–4 at $\theta_0 = 75°$ (a), $\theta_0 = 60°$ (b), $\theta_0 = 45°$ (c).

solution, as already carried out for the humped sleepers along a desert railway in Namibia (Riessberger, 2015).

CRediT authorship contribution statement

Marko Horvat: Conceptualization, Methodology, Formal analysis, Writing – original draft. **Luca Bruno:** Conceptualization, Methodology, Writing – original draft, Writing – review & editing. **Sami Khris:** Conceptualization, Methodology.

Declaration of competing interest

The authors declare that they have no known competing financial interests or personal relationships that could have appeared to influence the work reported in this paper.

Data availability

Data will be made available on request.

References

Araújo, A.D., Parteli, E.J.R., Pöschel, T., Andrade, J.S., Herrmann, H.J., 2013. Numerical modeling of the wind flow over a transverse dune. Sci. Rep.-Nat. 3 (2858), URL: https://www.nature.com/articles/srep02858.
Blocken, B., Carmeliet, J., Stathopoulos, T., 2007. CFD evaluation of wind speed conditions in passages between parallel buildings - effect of wall-function roughness modifications for the atmospheric boundary layer flow. J. Wind Eng. Ind. Aerodyn. 95 (9–11), 941–962. http://dx.doi.org/10.1016/j.jweia.2007.01.013.
Bruno, L., Fransos, D., 2015. Sand transverse dune aerodynamic: 3D coherent flow structures from a computational study. J. Wind Eng. Ind. Aerodyn. 147, 291–301. http://dx.doi.org/10.1016/j.jweia.2015.07.014.

Bruno, L., Fransos, D., Lo Giudice, A., 2018a. Solid barriers for windblown sand mitigation: Aerodynamic behavior and conceptual design guidelines. J. Wind Eng. Ind. Aerodyn. 173, 79–90. http://dx.doi.org/10.1016/j.jweia.2017.12.005.
Bruno, L., Horvat, M., Raffaele, L., 2018b. Windblown sand along railway infrastructures: A review of challenges and mitigation measures. J. Wind Eng. Ind. Aerodyn. 177, 340–365. http://dx.doi.org/10.1016/j.jweia.2018.04.021.
Cabral, B., Leedom, L.C., 1993. Imaging vector fields using line integral convolution. In: SIGGRAPH, Vol. 93. ACM Press, New York, USA, pp. 263–270. http://dx.doi.org/10.1145/166117.166151.
Cebeci, T., Bradshaw, P., 1977. Momentum Transfer in Boundary Layers. Wash DC Hemisphere Publ Corp N Y McGraw-Hill Book Co, URL: https://www.worldcat.org/title/momentum-transfer-in-boundary-layers/oclc/1036773246.
Cheng, J., Lei, J., Li, S., Wang, H., 2016a. Disturbance of the inclined inserting-type sand fence to wind–sand flow fields and its sand control characteristics. Aeolian Res. 21, 139–150. http://dx.doi.org/10.1016/j.aeolia.2016.04.008.
Cheng, J., Lei, J., Li, S., Wang, H., 2016b. Effect of hanging-type sand fence on characteristics of wind-sand flow fields. Wind Struct. 22 (5), 555–571. http://dx.doi.org/10.12989/was.2016.22.5.555.
Cheng, J., Xue, C., 2014. The sand-damage-prevention engineering system for the railway in the desert region of the Qinghai-Tibet plateau. J. Wind Eng. Ind. Aerodyn. 125, 30–37. http://dx.doi.org/10.1016/j.jweia.2013.11.016.
Dölçek, T., 2014. Mechanical behavior of polyurethane stabilized fouled ballast (PSFB). Geological Engineering at the University of Wisconsin, URL: http://minds.wisconsin.edu/bitstream/handle/1793/69518/MS_Thesis_Dolcek_Tolga.pdf.
Dong, Z., Chen, G., He, X., Han, Z., Wang, X., 2004. Controlling blown sand along the highway crossing the Taklimakan desert. J. Arid Environ. 57 (3), 329–344. http://dx.doi.org/10.1016/j.jaridenv.2002.02.001.
EN 1991-1-4, 2005. Eurocode 1: Actions on structures - Part 1-4: General actions - wind actions. European Committee for Standardization.
Esmaeili, M., Aela, P., Hosseini, A., 2017. Experimental assessment of cyclic behavior of sand-fouled ballast mixed with tire derived aggregates. Soil Dyn. Earthq. Eng. 98, 1–11. http://dx.doi.org/10.1016/j.soildyn.2017.03.033.
Faccoli, M., Petrogalli, C., Lancini, M., Ghidini, A., Mazzù, A., 2018. Effect of desert sand on wear and rolling contact fatigue behaviour of various railway wheel steels. Wear 396–397, 146–161. http://dx.doi.org/10.1016/j.wear.2017.05.012.
Horvat, M., Bruno, L., Khris, S., 2021. CWE study of wind flow around railways: Effects of embankment and track system on sand sedimentation. J. Wind Eng. Ind. Aerodyn. 208, 104476. http://dx.doi.org/10.1016/j.jweia.2020.104476.
Horvat, M., Bruno, L., Khris, S., Raffaele, L., 2020. Aerodynamic shape optimization of barriers for windblown sand mitigation using CFD analysis. J. Wind Eng. Ind. Aerodyn. 197, http://dx.doi.org/10.1016/j.jweia.2019.104058.
Jackson, D.W.T., Beyers, J.H.M., Delgado-Fernandez, I., Baas, A.C.W., Cooper, J.A.G., Lynch, K., 2013. Airflow reversal and alternating corkscrew vortices in foredune wake zones during perpendicular and oblique offshore winds. Geomorphology 187 (1), 86–93. http://dx.doi.org/10.1016/j.geomorph.2012.12.037.
Jackson, D.W.T., Beyers, J.H.M., Lynch, K., Cooper, J.A.G., Baas, A.C.W., Delgado-Fernandez, I., 2011. Investigation of three-dimensional wind flow behaviour over coastal dune morphology under offshore winds using computational fluid dynamics (CFD) and ultrasonic anemometry. Earth Surf. Process. Landf. 36 (8), 1113–1124. http://dx.doi.org/10.1002/esp.2139.
Keene, A., Edil, T., Tinjum, J., 2012. Mitigating Ballast Fouling and Enhancing Rail Freight Capacity. Technical Repor CFIRE 04-07, National Center for Freight and Infrastructure Research and Education, University of Winsconsin-Madison, URL: http://www.wistrans.org/cfire/documents/FR_CFIRE0407.pdf.
Kóllmann, J., 2013. Railway operations under harsh environmental conditions – sand, dust and humidity problems and technical solutions / mitigation measures. In: AHK Workshop Be a Partner of Qatar Rail, Berlin. URL: http://docplayer.net/22407097-Railway-operations-under-harsh-environmental-conditions.html.
Launder, B.E., Spalding, D.B., 1974. The numerical computation of turbulent flows. Comput. Methods Appl. Mech. Engrg. 3 (2), 269–289. http://dx.doi.org/10.1016/0045-7825(74)90029-2.

Lima, I., Araújo, A.D., Parteli, E.J.R., Herrmann, H.J., 2017. Optimal array of sand fences. Sci. Rep. 7, http://dx.doi.org/10.1038/srep45148.

Liu, B., Qu, J., Zhang, W., Qian, G., 2011. Numerical simulation of wind flow over transverse and pyramid dunes. J. Wind Eng. Ind. Aerodyn. 99 (8), 879. http://dx.doi.org/10.1016/j.jweia.2011.06.007.

Lo Giudice, A., Nuca, R., Preziosi, L., Coste, N., 2019. Wind-blown particulate transport: A review of computational fluid dynamics models. Math. Eng. 1 (3), 508–547. http://dx.doi.org/10.3934/mine.2019.3.508.

Lo Giudice, A., Preziosi, L., 2020. A fully Eulerian multiphase model of windblown sand coupled with morphodynamic evolution: Erosion, transport, deposition, and avalanching. Appl. Math. Model. 79, 68–84. http://dx.doi.org/10.1016/j.apm.2019.07.060.

Menter, F.R., 1994. Two-equation eddy-viscosity turbulencemodels for engineering applications. AIAA J. 32 (8), 269–289. http://dx.doi.org/10.2514/3.12149.

Menter, F.R., Kuntz, M., Langtry, R., 2003. Ten years of industrial experience with the SST turbulence model. In: Hanjalić, K., Nagano, Y., Tummers, J. (Eds.), Proceedings of the Fourth International Symposium on Turbulence, Heat and Mass Transfer. In: Turbulence Heat and Mass Transfer Series, vol. 4, Begell House, Antalya, Turkey, p. 1208, URL: https://www.researchgate.net/publication/228742295_Ten_years_of_industrial_experience_with_the]_SST_turbulence_model.

Merino, P., 2014. Arabia saudi: Un reto exigente para la internacionalización de la tecnología española. Lineas 80 (58–67), URL: http://www.adif.es/es_ES/comunicacion_y_prensa/doc/UltimoNumero.pdf.

Moyan, Z., Hong, X., Nadakatti, M.M., Feng, J., Guangpeng, L., 2020. Track structure failure caused by sand deposition: Simulation and experimentation. Aeolian Res. 43, http://dx.doi.org/10.1016/j.aeolia.2020.100578.

Noguchi, Y., Suzuki, M., Baker, C., Nakade, K., 2019. Numerical and experimental study on the aerodynamic force coefficients of railway vehicles on an embankment in crosswind. J. Wind Eng. Ind. Aerodyn. 184, 90–105. http://dx.doi.org/10.1016/j.jweia.2018.11.019.

Pointner, P., Joerg, A., Jaiswal, J., 2009. Definitive Guidelines on the Use of Different Rail Grades. Deliverable report D4.1.5GL, EU-Project "Innovative Track Systems" (Innotrack, TIP5-CT-2006-031415).

Raffaele, L., van Beeck, J., Bruno, L., 2021. Wind-sand tunnel testing of surface-mounted obstacles: Similarity requirements and a case study on a sand mitigation measure. J. Wind Eng. Ind. Aerodyn. 214, 104653. http://dx.doi.org/10.1016/j.jweia.2021.104653.

Raffaele, L., Bruno, L., Pellerey, F., Preziosi, L., 2016. Windblown sand saltation: A statistical approach to fluid threshold shear velocity. Aeolian Res. 23, 79–91. http://dx.doi.org/10.1016/j.aeolia.2016.10.002.

Raffaele, L., Coste, N., Glabeke, G., 2022. Life-cycle performance and cost analysis of sand mitigation measures: Toward a hybrid experimental-computational approach. J. Struct. Eng. (United States) 148 (7), 04022082. http://dx.doi.org/10.1061/(ASCE)ST.1943-541X.0003344.

Ramon-Rosales, R., 1995. Modellversuchen mit neuartigen schwellen zur reduzierung der verwehungsgefahr von eisenbahngleisen in gegenden mit flugsand. Graz University of Technology.

Richards, P.J., Norris, S.E., 2011. Appropriate boundary conditions for computational wind engineering models revisited. J. Wind Eng. Ind. Aerodyn. 99 (4), 257–266. http://dx.doi.org/10.1016/j.jweia.2010.12.008.

Riessberger, K., 2015. Heavy haul in sand environment. In: IHHA 2015 Conference, Perth, Australia. URL: https://docplayer.net/144777747-Heavy-haul-in-sand-environment.html.

Riessberger, K., Guggenberger, E., Ossberger, H., 2014. Sleepers having elevated rail fastening as protection against sand coverage, wo2014165871. URL: https://patentscope.wipo.int/search/en/detail.jsf?docId=WO2014165871.

Riessberger, K., Swanepoel, W., 2005. Specialised sleepers combat sand. Railw. Gaz. Int. 555, URL: https://trid.trb.org/view.aspx?id=789500.

Sarafrazi, V., Reza Talaee, M., 2019. Numerical simulation of sand transfer in wind storm using the Eulerian-Lagrangian two-phase flow model. Eur. Phys. J. E 42 (4), 1–13. http://dx.doi.org/10.1140/epje/i2019-11809-8.

Sarafrazi, V., Reza Talaee, M., 2020. Comparing performances of a triangular embankment and a rigid wall-type barrier in sandstorms using simulation and a wind tunnel test. Eur. Phys. J. E 43, 74. http://dx.doi.org/10.1140/epje/i2020-11996-1.

Sobanski, A., 2018. Etihad Rail Stage 2 & 3 Project, Appendix 19 — Wind Blown Sand Mitigation. Technical Report.

Sweby, P.K., 1984. High resolution schemes using flux limiters for hyperbolic conservation laws. SIAM J. Numer. Anal. 21, 995–1011, URL: https://www.jstor.org/stable/2156939.

Tsoar, H., Parteli, E.J.R., 2016. Bidirectional winds, barchan dune asymmetry and formation of seif dunes from barchans: a discussion. Environ. Earth Sci. 75, 1237. http://dx.doi.org/10.1007/s12665-016-6040-4.

van der Merwe, J., 2013. T-track system. URL: http://ttracksaudi.com.

Wang, K., Jiang, J., Zhang, W., 1989. Establishment of protective system and its ecological benefit along both sides of jing-tong railway. J. Desert Res. 9 (3), 1–12.

Weller, H., Tabor, G., Jasak, H., Fureby, C., 1998. A tensorial approach to computational continuum mechanics using object-oriented techniques. Comput. Phys. 12, 620–631. http://dx.doi.org/10.1063/1.168744.

Xie, S., Qu, J., Lai, Y., Pang, Y., 2015. Formation mechanism and suitable controlling pattern of sand hazards at honglianghe river section of qinghai–tibet railway. Nat. Hazards 76 (2), 855–871. http://dx.doi.org/10.1007/s11069-014-1523-7.

Zakeri, J.A., 2012. Investigation on railway track maintenance in sandy-dry areas. Struct. Infrastruct. Eng.: Mainten. Manag. Life-Cycle Des. Perform. 8 (2), 135–140. http://dx.doi.org/10.1080/15732470903384921.

Zakeri, J.A., Esmaeili, M., Fathali, M., 2011. Evaluation of humped slab track performance in desert railways. Proc. Inst. Mech. Eng. F 225 (6), 566–573. http://dx.doi.org/10.1177/0954409711403677.

Zakeri, J., Fathi, A., 2017. Analysis the influence of different forms of geometric humps on sand track crossing the desert using the fluent simulation software. Transp. Res. 14 (2), 349–362.

Zhang, J., Cui, E., Fu, G., 1995. Investigation of the flow field and the starting conditions of wind-induced erosion of the railway embankment. J. Wind Eng. Ind. Aerodyn. 54–55, 573–581. http://dx.doi.org/10.1016/0167-6105(94)00073-M.

Zhang, D., Narteau, C., Rozier, O., Courrech du Pont, S., 2012. Morphology and dynamics of star dunes from numerical modelling. Nat. Geosci. 5, 463–467. http://dx.doi.org/10.1038/ngeo1503.

Zhang, J., Wang, J., Tan, X., Gao, G., Xiong, X., 2019. Detached eddy simulation of flow characteristics around railway embankments and the layout of anemometers. J. Wind Eng. Ind. Aerodyn. 193, http://dx.doi.org/10.1016/j.jweia.2019.103968.